Phonon Lifetime Observation in Epitaxial ScN Film with Inelastic X-Ray Scattering Spectroscopy

H. Uchiyama,[1] Y. Oshima,[2] R. Patterson,[3] S. Iwamoto,[4] J. Shiomi,[4] and K. Shimamura[2]
[1]*Research and Utilization Division, Japan Synchrotron Radiation Research Institute (JASRI), SPring-8, 1-1-1 Koto, Sayo, Hyogo 679-5198, Japan*
[2]*Optical Single Crystals Group, Environment and Energy Materials Research Division, National Institute for Materials Science, 1-1 Namiki, Tsukuba, Ibaraki 305-0044, Japan*
[3]*School of Photovoltaic and Renewable Energy Engineering, University of New South Wales, Sydney 2052, Australia*
[4]*Department of Mechanical Engineering, The University of Tokyo, Bunkyo, Tokyo 113-8656, Japan*

(Received 18 December 2017; revised manuscript received 21 March 2018; published 7 June 2018)

Phonon-phonon scattering dominates the thermal properties in nonmetallic materials, and it directly influences device performance in applications. The understanding of the scattering has been progressing using computational approaches, and the direct and systematic observation of phonon modes that include momentum dependences is desirable. We report experimental data on the phonon dispersion curves and lifetimes in an epitaxially grown ScN film using inelastic x-ray scattering measurements. The momentum dependence of the optical phonon lifetimes is estimated from the spectral width, and the highest-energy phonon mode around the zone center is found to possess a short lifetime of 0.21 ps. A comparison with first-principles calculations shows that our observed phonon lifetimes are quantitatively explained by three-body phonon-phonon interactions.

DOI: 10.1103/PhysRevLett.120.235901

Thermal management plays an important role in semiconductor devices with continued advances in miniaturization to the nanoscale. In power devices, for example, local heating by the hot-electrons degrades the performance [1]. Another example can be seen in applications for energy harvesting devices, where heat is recycled as energy [2,3]. In the case of polar semiconductors, phonon properties are correlated to the thermal properties, which leads to the following consequences. First, the highest energy [longitudinal optical (LO)] phonon mode at the zone center dominates the heat dissipation process of hot carriers, owing to the Frölich interaction. The thermalization rates can, hence, be reduced by the reabsorption of these high energy phonons that couple strongly to electrons [1]. Reducing the LO phonon lifetime can avoid local heating, where energy is returned to charge carriers and phonon decay is inhibited, leading to devices with low energy consumption and high performance. On the other hand, prolonging the LO phonon lifetime can be helpful in the hot-carrier photovoltaic concept [3–6]. Detailed knowledge of the available vibrational modes is central to interpreting ultrafast relaxation and energy dissipation processes [4,5]. Second, the velocities and lifetimes of all phonon modes determine the lattice thermal conductivity, which in general leads to heat dissipation in devices [7]. This lattice thermal conductivity is an important parameter to evaluate the thermoelectric figure of merit (ZT), which determines the properties of thermoelectric devices [2].

Recent developments in first-principles density-functional theory (DFT) calculations now provide both dispersions and lifetimes of all phonon modes with the momentum dependence, and thermal conductivities in many materials can also be estimated precisely using these phonon properties [8–10]. Experimentally, recent inelastic neutron or x-ray scattering measurements reveal correlations between thermal conductivities and phonon properties for several thermoelectric materials (such as PbTe [11], UO_2 [12], $AgSbTe_2$ [13], Na_xCoO_2 [14], and clathrate BaGeAu [15]). These studies have been confined to bulk crystalline materials, mainly owing to the long penetration depth of the neutron, and no detailed study has been reported for epitaxial films, the most common forms in device applications. Raman scattering is a well-known method, which detects the phonon energy and lifetime of the epitaxial films (for example, for wurtzite InN films [16–18]). However, this method can only measure some optical phonon modes at the zone center in the first-order scattering, and it gives no information about the phonon dispersion relations. Inelastic x-ray scattering (IXS) is a unique technique that reveals the phonon dispersion curves in films [19–22], but no detailed observation of the phonon lifetime, that includes temperature and momentum dependence, has been investigated.

ScN, a semiconductor with an electronic band gap of 0.9 eV [23], is a promising thermoelectric candidate among the nitride semiconductors [2,24–27]. Since this material is normally obtained as epitaxial films, the fundamental elastic properties and the origin of the low thermal conductivity are yet unknown. This material has a rocksalt structure, in which no phonon modes should be observed in the first-order Raman scattering. Some high-order Raman scattering measurements have been conducted [28–32], but the results only show the phonon energy at some points in the Brillouin zone. In this Letter, we present detailed and direct observations of phonon energies and lifetimes in an epitaxial ScN film as a function of momentum, in order to elucidate both the harmonic and anharmonic contributions of the phonon modes present in the material. After optimizing the incident angle with respect to the surface of the film (α in Fig. 1(a). We chose $\alpha = 1.1 - 1.7°$ in the measurements, see Supplemental Material for the detailed optimization [33]), we obtained information only from the ScN film, without artifacts from the substrate. The experimental results agree with the DFT calculations; i.e., the phonon energies are described by the harmonic approximation. The phonon lifetimes, estimated from the spectral linewidth, are well explained by the lowest-order (cubic) anharmonic phonon-phonon interaction. In addition, thermal conductivity derived from the calculations well reproduces that of this film, but much higher than those in previous studies [24,26,27], suggesting that defects and impurities also serve a vital role in the thermal conductivity.

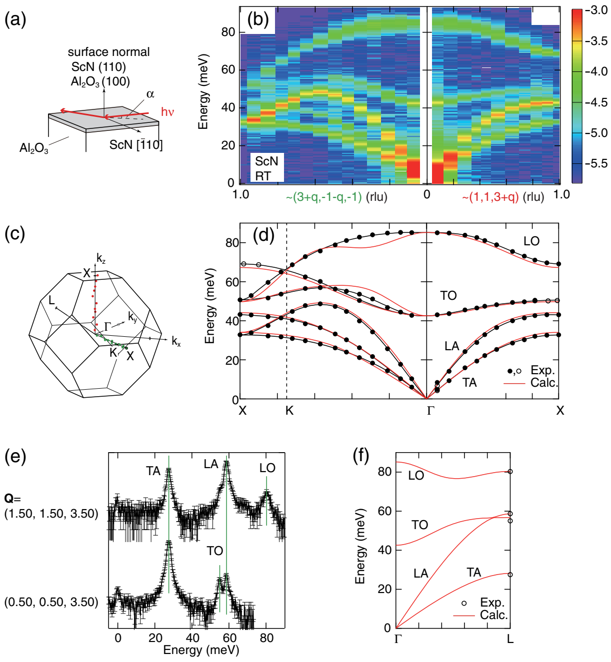

FIG. 1. Phonon dispersion relations of ScN. (a) Experimental configuration for the IXS measurements. (b) IXS spectra on a logarithmic scale, obtained for $\mathbf{Q} \sim (3 + q, -1 - q, -1)$ (left) and $(1, 1, 3 + q)$ (right). (c) The Brillouin zone of the ScN crystal. The green and red solid circles represent the exact measured $\mathbf{q}$ for the left and right panels in (b), respectively. (d) Peak positions estimated from (b) (black solid circles) in the reduced Brillouin zone and corresponding phonon dispersion curves in the DFT calculations (red lines). Black lines are guides to eyes. Additional peak positions estimated from the spectra for $\mathbf{Q} \sim (4, q, 0)$, $(3 + q, -1, -1)$, and $(2 - q, 2 - q, 4)$ are depicted as black open circles. (e) IXS spectra (on a logarithmic scale) at the L point. (f) Calculated phonon dispersion curve in the $[qqq]$ direction (red). The peak positions in (e) are displayed as black open circles.

The ScN (110) film, which has a thickness of 40 μm, was grown by a hydride vapor phase epitaxy (HVPE) method on a sapphire (Al_2O_3) (100) (m-plane) substrate [34]. The film measured has carrier of $n = 1.07 \times 10^{19}$ cm^{-3} (electron) and mobility of $\mu = 164$ cm^2/V/s at room temperature (RT, $T \sim 300$ K). The carrier of ScN originates from the defects and impurities, and the present carrier concentration is much smaller than the previous literature [25–27], indicating that the sample is of good crystal quality [34]. IXS measurements were performed on the BL35XU beam line at the SPring-8 synchrotron facility [41]. An incident x-ray energy of $h\nu = 21.747$ keV, which corresponds to Si(11 11 11) reflection, gives an energy resolution of $1.4 - 1.7$ meV. In the present setup, each analyzer has a momentum resolution of 0.9 nm^{-1}, or $\Delta\mathbf{Q} \sim (0.07, 0.07, 0.01) - (0.05, 0.05, 0.06)$ (depending on the geometry) for ScN. In estimating the elastic constants, the measurements with a better resolution of 0.4 nm^{-1} were also achieved. Overall uncertainty in determining the IXS peak positions is at around ±0.3 meV. The DFT calculations, with a cutoff energy of 20 Hartree, were produced using the local density approximation (LDA) based on the projector-augmented-wave (PAW) method, as implemented in the ABINIT package [42,43]. The lattice parameters were optimized under the calculations at a zero pressure condition. In calculating the harmonic and anharmonic contribution, PHONOPY and PHONO3PY codes [10] were used. The quadratic and cubic interatomic potential were obtained by a $2 \times 2 \times 2$ (64 atoms) supercell approach with finite atomic displacements of 0.03 Å. It should be noted that the nonanalytical term [44], which defines LO-TO (transverse optical) splitting, was adjusted to reproduce the experimentally observed LO-TO splitting at around Γ in the present calculations. The DFT calculations tend to underestimate the splitting [18], perhaps due to the underestimation of the (electronic) band gap; the present calculations suggest that ScN has no (electronic) band gap, though in reality ScN has an (indirect) band gap [23,45].

Figure 1(b) shows the IXS spectra on a logarithmic scale for $\mathbf{Q} \sim (3 + q, -1 - q, -1)$ (left panel) and $(1, 1, 3 + q)$ (right) at RT. These momenta $\mathbf{Q}$ mostly correspond to $\mathbf{q} = (q\bar{q}0)$ and $(00q)$ in the reduced Brillouin zone ($\mathbf{Q} = \mathbf{q} + \mathbf{G}, \mathbf{G}$ is a reciprocal lattice vector) and multiple nearby $\mathbf{q}$ points are simultaneously sampled by the detector array, leading to efficient data collection. The exact $\mathbf{q}$ values are displayed as green and red points in Fig. 1(c) (also see Supplemental Material for the detailed information of $\mathbf{Q}$ [33]). The peak positions in Fig. 1(b) are determined using Voigt peak fitting and plotted in Fig. 1(d) as black solid circles. Some of the peak intensities are too weak to be identified, as seen in Fig. 1(b), and some of the acoustic phonon modes do not show the correct peak position, owing to the overlapping of LA (longitudinal acoustic) and TA (transverse acoustic) and a deviation from the high symmetry lines. To complete the estimates of the dispersion relations, additional measurements were performed in different Brillouin zones [$\mathbf{G} = (400)$ and (224), not shown] and the fitting results are depicted as black open circles in Fig. 1(d). It is evident from Fig. 1(d) that all experimental peak positions can be assigned to ScN phonon modes. For example, in the [001] direction, the phonon consists of four modes, TA, LA, TO, and LO. The red lines in Fig. 1(d) indicate the phonon dispersion in the DFT calculations along the high-symmetry lines, which reproduces the measurements remarkably well (black). For further confirmation, we also observed the phonon modes at $\mathbf{Q} = (1.50, 1.50, 3.50)$ and (0.50, 0.50, 3.50), which correspond to the L point [Fig. 1(e)], supporting the agreement between observation and calculations, as seen in Fig. 1(f). The elastic constants at RT were determined from spectra around Γ through the Christoffel equation (see Supplemental Material for details [33]). Experimentally obtained elastic constants are $C_{11} = 384(5)$, $C_{12} = 107(5)$, and $C_{44} = 178(5)$ GPa, that fairly agree with the present calculations: $C_{11} = 442$, $C_{12} = 238$, and $C_{44} = 160$ GPa.

The phonon lifetime due to phonon-phonon scattering is correlated to the imaginary part of the phonon self-energy $\Sigma_{\mathbf{q},j}(\omega)$ (for the jth phonon mode at $\mathbf{q}$), and in a simple approximation this $\mathrm{Im}\Sigma_{\mathbf{q},j}(\omega)$ can be regarded as a constant, $\mathrm{Im}\Sigma^{\circ}_{\mathbf{q},j} = \mathrm{Im}\Sigma_{\mathbf{q},j}(\omega_{\mathbf{q},j})$, which is given as

$$\mathrm{Im}\Sigma^{\circ}_{\mathbf{q},j} = \frac{18\pi}{\hbar^2}\sum_{\mathbf{q}_1,\mathbf{q}_2}|\Psi(-\mathbf{q}_0,\mathbf{q}_1,\mathbf{q}_2)|^2(n_1+n_2+1)\delta_{\omega_0,\omega_1+\omega_2} - 2|\Psi(-\mathbf{q}_0,\mathbf{q}_1,-\mathbf{q}_2)|^2(n_1-n_2)\delta_{\omega_0,\omega_1-\omega_2}. \tag{1}$$

Here, n_i is the Bose-Einstein distribution function for the phonon mode ω_i ($= \omega_{\mathbf{q},j}$), and

$$\Psi(\mathbf{q}_0,\mathbf{q}_1,\mathbf{q}_2) = \frac{1}{6\sqrt{N}}\sum\sqrt{\frac{\hbar^3}{8m_0m_1m_2\omega_0\omega_1\omega_2}}\sum\mathbf{e}_0\otimes\mathbf{e}_1\otimes\mathbf{e}_2 \vdots \phi^{(3)} \times \exp(i\mathbf{q}_0\cdot\mathbf{r}_0 + i\mathbf{q}_1\cdot\mathbf{r}_1 + i\mathbf{q}_2\cdot\mathbf{r}_2)\delta_{\mathbf{q}+\mathbf{q}_1+\mathbf{q}_2,\mathbf{G}}. \tag{2}$$

$\phi^{(3)}$ is the cubic interatomic potential, and $\mathbf{e}_i$, m_i, $\mathbf{r}_i$ are the eigenvector, mass, and position of an atom for the phonon mode ω_i, respectively. Equations (1) and (2) indicate that $\mathrm{Im}\Sigma^{\circ}_{\mathbf{q},j}$ has nonzero contribution only in a decay (down-conversion) process;

$$\omega_0 = \omega_1 + \omega_2, \qquad \mathbf{q}_0 + \mathbf{G} = \mathbf{q}_1 + \mathbf{q}_2, \tag{3a}$$

and in a merging (up-conversion) process;

$$\omega_0 + \omega_1 = \omega_2, \qquad \mathbf{q}_0 + \mathbf{q}_1 = \mathbf{q}_2 + \mathbf{G}. \tag{3b}$$

Following the fitting method described in the Supplemental Material [33], the extracted phonon linewidth of the LO mode in the [001] direction, $2\mathrm{Im}\Sigma^{\circ}_{(00q),\mathrm{LO}}$, is depicted in Fig. 2(d) as black solid circles. Some of the observed spectra (dots) and fitted results (lines) are shown in Figs. 2(a), 2(b), and 2(c). The phonon linewidth determined from the DFT calculations [red in Fig. 2(d)] compares excellently with the experimental results. The calculations indicate that the phonon linewidth in this [00q] direction is caused only by the phonon decay process. The details of the phonon scattering, which contributes to the phonon linewidth, can be seen in Figs. 2(e), 2(f), and 2(g) for several $\mathbf{q}$. In each Fig., decay phonons are displayed as black dots. Each momentum corresponding to a decay or product phonon is represented by the position of the dots, while the scattering intensity is indicated by the dot size.

Similar reasoning applies to the TO mode in the [00q] direction, as seen in Fig. 3. Resemblance between the calculations (red) and measurements (black) can be easily found in Fig. 3(d). The calculations suggest that the

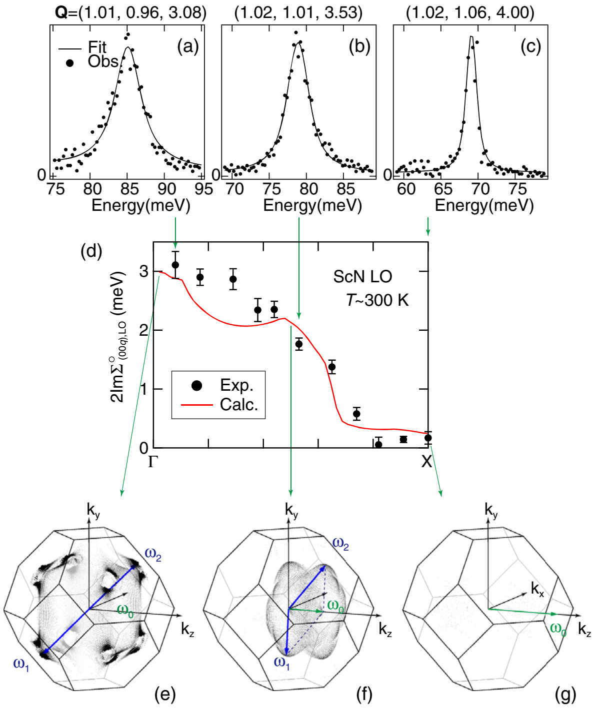

FIG. 2. LO phonon linewidth of ScN along the [00q] direction. (a)–(c) IXS spectra at $\mathbf{q} \sim (00q)$ measured at RT. The lines are fits to a function described in the Supplemental Material. (d) Experimentally obtained phonon linewidth (black solid circles) and linewidth in the DFT calculations (at $T = 300$ K, red line). (e)–(g) Plot of the calculated decay phonon [ω_1 and ω_2 in Eq. (3a)]. Momenta of decay phonons ($\mathbf{q}_1$ and $\mathbf{q}_2$) are indicated by the position of the black dots. The blue arrows in (e) and (f) show one pair of decay phonons from the original (00q) phonon (ω_0, green arrow).

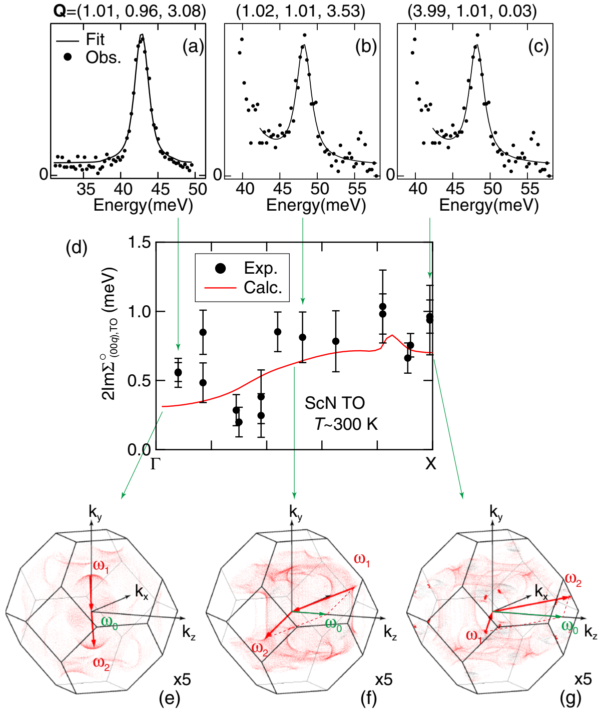

FIG. 3. TO phonon linewidth of ScN in $[00q]$. (a)–(c) IXS spectra at $\mathbf{q} \sim (00q)$ measured at RT. (d) Experimentally obtained phonon linewidth (black solid circles) and linewidth in the DFT calculations (at $T = 300$ K, red line). (e)–(g) Plot of the calculated decay phonons (black dots) and phonons involved in the merging process (red dots). Momenta of the phonons involved in the scattering processes ($\pm\mathbf{q}_1$ and $\mathbf{q}_2$ for the decay or merging process) are indicated by the position, and the scattering intensity is indicated by the size, which was enlarged by a factor of 5 compared to that in Fig. 2. The red arrows display one pair of phonons involved in the merging process [ω_1 and ω_2 in Eq. (3b)], and the green arrow shows the original phonon (ω_0).

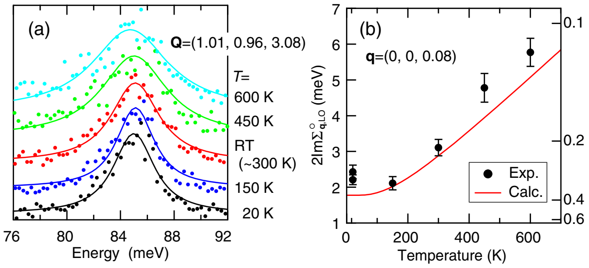

FIG. 4. Temperature dependence of LO phonon linewidth of ScN at $\mathbf{Q} = (1.01, 0.98\,3.08)$. (a) Temperature dependent IXS spectra. (b) Comparison of the calculations (red line) and measurements (black circles) in the reduced Brillouin zone.

merging process dominates the decay process in TO, in contrast to LO. Technically speaking, as seen in Fig. 3(e), calculations predict that the decay process rarely happens at the zone center (0.1% of the total scattering), but it increases for a higher $\mathbf{q}$ [10.5% in Fig. 3(f), 22.1% in Fig. 3(g)].

When rapid reabsorption of LO phonons by charge carriers takes place before the LO phonon decay at the zone center, phonon bottleneck effects can be enhanced. Figure 2(e) shows that the decay phonons predominantly appear around the L points. This decay process is something similar to the Ridley channel [46], where LO phonons decay into acoustic and TO phonon modes (LO → LA/TA + TO). However, the process obtained here is more complicated. The decay phonons no longer have pure transverse or longitudinal polarization, because they are not on the high-symmetry lines. Furthermore, the decay process can be also considered to be Klemens-like (LO → 2LA/TA) [47], because the LA and TO modes have similar energy at L [Fig. 1(f)]. This LO linewidth increases with temperature [Fig. 4(a), and the derived phonon linewidth is depicted in black solid circles in Fig. 4(b)]. Again, the observation is well explained by the calculations [red line in Fig. 4(b)]. A similar temperature dependence of linewidth can be found, for example, in the Raman scattering measurements of wurtzite InN for the highest E_1(LO) phonon mode [18]. In Ref. [18], a large temperature-dependent peak shift of this mode was also observed (~2.5 meV shift between $T = 80$ and 600 K), in contrast to ScN (0.2 ± 0.3 meV between $T = 20$ and 600 K [Fig. 4(a)]). This difference may be caused by the structural differences [wurtzite (InN) and rocksalt (ScN)]. In fact, in MgO, another rocksalt structure, the peak position of the LO mode is mostly unchanged in this temperature range [48].

The lattice thermal conductivity, $\kappa^{(2)}$ (rank 2 tensor), is estimated by solving the linearized phonon Boltzmann equation using the single-mode relaxation time, $\tau^{\circ}_{\mathbf{q},j}$ $(= \hbar/2\mathrm{Im}\Sigma^{\circ}_{\mathbf{q},j})$;

$$\kappa^{(2)} = \frac{1}{NV_0}\sum_{\mathbf{q},j} C_{\mathbf{q},j}\mathbf{v}_{\mathbf{q},j} \otimes \mathbf{v}_{\mathbf{q},j}\tau^{\circ}_{\mathbf{q},j}. \tag{4}$$

Here, NV_0 is the volume of the solid, $[\mathbf{v}_{\mathbf{q},j}]_\alpha = \partial\omega_{\mathbf{q},j}/\partial q_\alpha$ is the group velocity, and $C_{\mathbf{q},j}$ is the heat capacity. Specifically, $\kappa^{(2)}$ of ScN is isotropic due to the crystal symmetry, and the scalar thermal conductivity κ [$= \mathrm{tr}(\kappa^{(2)})/3$] can be defined. The calculated lattice thermal conductivity of ScN is $\kappa_{\mathrm{ScN}} =$ 43 W/m/K at $T = 300$ K and 21 W/m/K at $T = 600$ K, which shows a good agreement with the experimentally obtained value, $\kappa_{\mathrm{ScN}} = 36.4$ W/m/K at RT (see Supplemental Material for the detailed information [33]). These values are close to those of MgO ($\kappa_{\mathrm{MgO}} = 51$ W/m/K at $T = 300$ K and 23 W/m/K at $T = 600$ K [49,50]), which has the same structure and similar molar mass to ScN. Note that, the isotope effect seen in GaN [9] is expected to be negligible in ScN, because without any intentional incorporation of Sc and N isotopes, the content of these will be extremely small.

The previous literature reports significantly lower thermal conductivity of 10 – 20 W/m/K [24,26,27] than the present study, and this deviation is presumed to arise from the imperfectness of the crystals. Table I, which

TABLE I. Comparison of measured carrier (electron) concentration (n) and thermal conductivity (κ) of ScN at RT.

n (cm^{-3})	κ (W/m/K)	Reference
1.45×10^{21}	11.0	[27]
2.5×10^{20}	20.7	[26]
1.07×10^{19}	36.4	Present work

summarizes the results of the carrier and thermal conductivity measurements, including the present study, shows a negative correlation. Given the fact that the defects (such as nitrogen vacancies) and impurities (such as oxygen and chlorine) enhance the carrier concentration of ScN [25–27,34], and reduce the thermal conductivity in general [51], the negative correlation in Table I should be the results from the defects and impurities. This also indicates that enriching impurities and/or defects is effective to reduce thermal conductivity for thermoelectric applications. Furthermore, the good agreement between the present measurements and calculations testifies that the present sample is close to the ideal (perfect) crystal, that is supported by the lowest carrier concentration in Table I.

When the obtained results are compared to other nitrides, the LO phonon lifetime of ScN at RT is 0.21 ps near Γ [Fig. 4(b)], which is much shorter than the E_1(LO) phonon lifetimes of GaN (0.56 ps [52]) and InN (0.45 ps [18]). The rapid heat dissipation resulting from the short LO phonon lifetime may be useful in nitride power devices. Moreover, the ideal thermal conductivity for ScN (43 W/m/K at $T = 300$ K) is smaller than those for other nitrides (176 W/m/K for InN [53] and ~240 W/m/K for GaN [9]). Utilizing the low thermal conductivity, ScN is suitable for thermoelectric application as indicated in Refs. [2,24–27]. As discussed above, further reduction of the thermal conductivity may be possible with introducing more defects and impurities.

In summary, direct observations of the phonon dispersion relations and lifetimes of ScN have been made, with no additional (i.e., surface and substrate) contributions. All observed properties are consistent with the DFT calculations, and the optical phonon lifetime is well explained by the three-body phonon-phonon interaction. The experiments demonstrate the possibility of investigating thermal properties through phonon observation with momentum dependence. Eventually, this technique can be in general applied to epitaxial films, to help to reveal the correlation between the phonon and thermal properties, that provide guidelines in fabricating the next-generation devices with layered structures, such as thermoelectric, high power, and photovoltaic devices.

H. U. thanks I. Terasaki for helpful discussions. Measurements at SPring-8 were supported by the JASRI President's fund and performed under Proposals No. 2015A2030, No. 2015B1980, and No. 2016B1495.

[1] H. Morkoç, *Nitride Semiconductor Devices* (Wiley-VCH, Weinheim, 2013).
[2] A. Shakouri, Recent developments in semiconductor thermoelectric physics and materials, Annu. Rev. Mater. Res. **41**, 399 (2011).
[3] M. A. Green and S. P. Bremner, Energy conversion approaches and materials for high-efficiency photovoltaics, Nat. Mater. **16**, 23 (2017).
[4] J. Yang, X. Wen, H. Xia, R. Sheng, Q. Ma, J. Kim, P. Tapping, T. Harada, T. W. Kee, F. Huang, Y.-B. Cheng, M. Green, A. Ho-Baillie, S. Huang, S. Shrestha, R. Patterson, and G. Conibeer, Acoustic-optical phonon up-conversion and hot-phonon bottleneck in lead-halide perovskites, Nat. Commun. **8**, 14120 (2017).
[5] Y. Yang, D. P. Ostrowski, R. M. France, K. Zhu, J. van de Lagemaat, J. M. Luther, and M. C. Beard, Observation of a hot-phonon bottleneck in lead-iodide perovskites, Nat. Photonics **10**, 53 (2016).
[6] G. Conibeer, S. Shrestha, S. Huang, R. Patterson, H. Xia, Y. Feng, P. Zhang, N. Gupta, M. Tayebjee, S. Smyth, Y. Liao, S. Lin, P. Wang, X. Dai, and S. Chung, Hot carrier solar cell absorber prerequisites and candidate material systems, Sol. Energy Mater. Sol. Cells **135**, 124 (2015).
[7] S. Adachi, Lattice thermal conductivity of group-IV and III–V semiconductor alloys, J. Appl. Phys. **102**, 063502 (2007).
[8] K. Esfarjani and H. T. Stokes, Method to extract anharmonic force constants from first principles calculations, Phys. Rev. B **77**, 144112 (2008).
[9] L. Lindsay, D. A. Broido, and T. L. Reinecke, Thermal Conductivity and Large Isotope Effect in GaN from First Principles, Phys. Rev. Lett. **109**, 095901 (2012).
[10] A. Togo, L. Chaput, and I. Tanaka, Distributions of phonon lifetimes in Brillouin zones, Phys. Rev. B **91**, 094306 (2015).
[11] O. Delaire, J. Ma, K. Marty, A. F. May, M. A. McGuire, M.-H. Du, D. J. Singh, A. Podlesnyak, G. Ehlers, M. D. Lumsden, and B. C. Sales, Giant anharmonic phonon scattering in PbTe, Nat. Mater. **10**, 614 (2011).
[12] J. W. L. Pang, W. J. L. Buyers, A. Chernatynskiy, M. D. Lumsden, B. C. Larson, and S. R. Phillpot, Phonon Lifetime Investigation of Anharmonicity and Thermal Conductivity of UO_2 by Neutron Scattering and Theory, Phys. Rev. Lett. **110**, 157401 (2013); J. W. L. Pang, A. Chernatynskiy, B. C. Larson, W. J. L. Buyers, D. L. Abernathy, K. J. McClellan, and S. R. Phillpot, Phonon density of states and anharmonicity of UO_2, Phys. Rev. B **89**, 115132 (2014).
[13] J. Ma, O. Delaire, A. F. May, C. E. Carlton, M. A. McGuire, L. H. VanBebber, D. L. Abernathy, G. Ehlers, T. Hong, A. Huq, W. Tian, V. M. Keppens, Y. Shao-Horn, and B. C. Sales, Glass-like phonon scattering from a spontaneous nanostructure in $AgSbTe_2$, Nat. Nanotechnol. **8**, 445 (2013); J. Ma, O. Delaire, E. D. Specht, A. F. May, O. Gourdon, J. D. Budai, M. A. McGuire, T. Hong, D. L. Abernathy, G. Ehlers, and E. Karapetrova, Phonon scattering rates and atomic ordering in $Ag_{1-x}Sb_{1+x}Te_{2+x}$ (x=0, 0.1, 0.2) investigated with inelastic neutron scattering and synchrotron diffraction, Phys. Rev. B **90**, 134303 (2014).
[14] D. J. Voneshen, K. Refson, E. Borissenko, M. Krisch, A. Bosak, A. Piovano, E. Cemal, M. Enderle, M. J. Gutmann,

M. Hoesch, M. Roger, L. Gannon, A. T. Boothroyd, S. Uthayakumar, D. G. Porter, and J. P. Goff, Suppression of thermal conductivity by rattling modes in thermoelectric sodium cobaltate, Nat. Mater. **12**, 1028 (2013).

[15] P.-F. Lory, S. Pailhès, V. M. Giordano, H. Euchner, H. D. Nguyen, R. Ramlau, H. Borrmann, M. Schmidt, M. Baitinger, M. Ikeda, P. Tomeš, M. Mihalkovič, C. Allio, M. R. Johnson, H. Schober, Y. Sidis, F. Bourdarot, L. P. Regnault, J. Ollivier, S. Paschen, Y. Grin, and M. de Boissieu, Direct measurement of individual phonon lifetimes in the clathrate compound $Ba_{7.81}Ge_{40.67}Au_{5.33}$, Nat. Commun. **8**, 491 (2017).

[16] J. W. Pomeroy, M. Kuball, H. Lu, W. J. Schaff, X. Wang, and A. Yoshikawa, Phonon lifetimes and phonon decay in InN, Appl. Phys. Lett. **86**, 223501 (2005).

[17] X. D. Pu, J. Chen, W. Z. Shen, H. Ogawa, and Q. X. Guo, Temperature dependence of Raman scattering in hexagonal indium nitride films, J. Appl. Phys. **98**, 033527 (2005).

[18] N. Domènech-Amador, R. Cuscó, L. Artús, T. Yamaguchi, and Y. Nanishi, Raman scattering study of anharmonic phonon decay in InN, Phys. Rev. B **83**, 245203 (2011).

[19] H. Xia, R. Patterson, S. Smyth, Y. Feng, S. Chung, Y. Zhang, S. Shrestha, S. Huang, H. Uchiyama, S. Tsutsui, M. Sugiyama, A. Q. R. Baron, and G. Conibeer, Inelastic X-ray scattering measurements of III–V multiple quantum wells, Appl. Phys. Lett. **110**, 043102 (2017).

[20] M. Hoesch, T. Fukuda, J. Mizuki, T. Takenouchi, H. Kawarada, J. P. Sutter, S. Tsutsui, A. Q. R. Baron, M. Nagao, and Y. Takano, Phonon softening in superconducting diamond, Phys. Rev. B **75**, 140508(R) (2007).

[21] J. Serrano, A. Bosak, M. Krisch, F. J. Manjón, A. H. Romero, N. Garro, X. Wang, A. Yoshikawa, and M. Kuball, InN Thin Film Lattice Dynamics by Grazing Incidence Inelastic X-Ray Scattering, Phys. Rev. Lett. **106**, 205501 (2011).

[22] F. Caruso, M. Hoesch, P. Achatz, J. Serrano, M. Krisch, E. Bustarret, and F. Giustino, Nonadiabatic Kohn Anomaly in Heavily Boron-Doped Diamond, Phys. Rev. Lett. **119**, 017001 (2017).

[23] H. A. Al-Brithen, A. R. Smith, and D. Gall, Surface and bulk electronic structure of ScN(001) investigated by scanning tunneling microscopy/spectroscopy and optical absorption spectroscopy, Phys. Rev. B **70**, 045303 (2004).

[24] V. Rawat, Y. K. Koh, D. G. Cahill, and T. D. Sands, Thermal conductivity of (Zr,W)N/ScN metal/semiconductor multilayers and superlattices, J. Appl. Phys. **105**, 024909 (2009).

[25] S. Kerdsongpanya, N. V. Nong, N. Pryds, A. Žukauskaitė, J. Jensen, J. Birch, J. Lu, L. Hultman, G. Wingqvist, and P. Eklund, Anomalously high thermoelectric power factor in epitaxial ScN thin films, Appl. Phys. Lett. **99**, 232113 (2011).

[26] P. V. Burmistrova, J. Maassen, T. Favaloro, B. Saha, S. Salamat, Y. R. Koh, M. S. Lundstrom, A. Shakouri, and T. D. Sands, Thermoelectric properties of epitaxial ScN films deposited by reactive magnetron sputtering onto MgO(001) substrates, J. Appl. Phys. **113**, 153704 (2013).

[27] S. Kerdsongpanya, B. Sun, F. Eriksson, J. Jensen, J. Lu, Y. K. Koh, N. V. Nong, B. Balke, B. Alling, and P. Eklund, Experimental and theoretical investigation of $Cr_{1-x}Sc_xN$ solid solutions for thermoelectrics, J. Appl. Phys. **120**, 215103 (2016).

[28] G. Travaglini, F. Marabelli, R. Monnier, E. Kaldis, and P. Wachter, Electronic structure of ScN, Phys. Rev. B **34**, 3876 (1986).

[29] Z. Gu, J. H. Edgar, J. Pomeroy, M. Kuball, and D. W. Coffey, Crystal growth and properties of scandium nitride, J. Mater. Sci.: Mater. Electron. **15**, 555 (2004).

[30] B. Saha, G. Naik, V. P. Drachev, A. Boltasseva, E. E. Marinero, and T. D. Sands, Electronic and optical properties of ScN and (Sc,Mn)N thin films deposited by reactive DC-magnetron sputtering, J. Appl. Phys. **114**, 063519 (2013).

[31] D. Gall, M. Stoehr, and J. E. Greene, Vibrational modes in epitaxial $Ti_{1-x}Sc_xN(001)$ layers: An *ab initio* calculation and Raman spectroscopy study, Phys. Rev. B **64**, 174302 (2001).

[32] T. R. Paudel and W. R. L. Lambrecht, Calculated phonon band structure and density of states and interpretation of the Raman spectrum in rocksalt ScN, Phys. Rev. B **79**, 085205 (2009).

[33] See Supplemental Material at http://link.aps.org/supplemental/10.1103/PhysRevLett.120.235901 for results of the x-ray diffraction measurements, methods extracting the phonon linewidth and elastic constants, detailed information of **Q**, and the procedure of the thermal conductivity measurements. This Supplemental Material includes Refs. [28,34–40].

[34] Y. Oshima, E. G. Víllora, and K. Shimamura, Hydride vapor phase epitaxy and characterization of high-quality ScN epilayers, J. Appl. Phys. **115**, 153508 (2014).

[35] S. Brennan, A. Munkholm, O. S. Leung, and W. D. Nix, X-ray measurements of the depth dependence of stress in gold films, Physica (Amsterdam) **283B**, 125 (2000).

[36] B. M. Murphy, H. Requardt, J. Stettner, J. Serrano, M. Krisch, M. Müller, and W. Press, Phonon Modes at the $2H$-$NbSe_2$ Surface Observed by Grazing Incidence Inelastic X-Ray Scattering, Phys. Rev. Lett. **95**, 256104 (2005).

[37] D. Waasmaier and A. Kirfel, New analytical scattering-factor functions for free atoms and ions, Acta Crystallogr. Sect. A **51**, 416 (1995).

[38] A. A. Maradudin and A. E. Fein, Scattering of neutrons by an anharmonic crystal, Phys. Rev. **128**, 2589 (1962).

[39] B. A. Auld, *Acoustic Fields and Waves in Solids* (Wiley, New York, 1973), Vol. 1.

[40] D. G. Cahill, Analysis of heat flow in layered structures for time-domain thermoreflectance, Rev. Sci. Instrum. **75**, 5119 (2004).

[41] A. Q. R. Baron, Y. Tanaka, S. Goto, K. Takeshita, T. Matsushita, and T. Ishikawa, An X-ray scattering beamline for studying dynamics, J. Phys. Chem. Solids **61**, 461 (2000).

[42] X. Gonze, J.-M. Beuken, R. Caracas, F. Detraux, M. Fuchs, G.-M. Rignanese, L. Sindic, M. Verstraete, G. Zerah, F. Jollet, M. Torrent, A. Roy, M. Mikami, Ph. Ghosez, J.-Y. Raty, and D. C. Allan, First-principles computation of material properties: the ABINIT software project, Comput. Mater. Sci. **25**, 478 (2002).

[43] H. Uchiyama, Potential asymmetry in antiferromagnetic $3d$ transition metal monoxides, Phys. Rev. B **85**, 014419 (2012).

[44] R. M. Pick, M. H. Cohen, and R. M. Martin, Microscopic theory of force constants in the adiabatic approximation, Phys. Rev. B **1**, 910 (1970).

[45] C. Li and D. Broido, Phonon thermal transport in transition-metal and rare-earth nitride semiconductors from first principles, Phys. Rev. B **95**, 205203 (2017).

[46] B. K. Ridley, The LO phonon lifetime in GaN, J. Phys. Condens. Matter **8**, L511 (1996).

[47] P. G. Klemens, Anharmonic decay of optical phonons, Phys. Rev. **148**, 845 (1966).

[48] K. Hisano and K. Toda, Temperature dependence of optical modes of vibration in MgO thin film, J. Phys. C **15**, 1111 (1982).

[49] D. G. Cahill, S.-M. Lee, and T. I. Selinder, Thermal conductivity of κ-Al_2O_3 and α-Al_2O_3 wear-resistant coatings, J. Appl. Phys. **83**, 5783 (1998).

[50] S. Stackhouse, L. Stixrude, and B. B. Karki, Thermal Conductivity of Periclase (MgO) from First Principles, Phys. Rev. Lett. **104**, 208501 (2010).

[51] N. A. Katcho, J. Carrete, Wu Li, and N. Mingo, Effect of nitrogen and vacancy defects on the thermal conductivity of diamond: An *ab initio* Green's function approach, Phys. Rev. B **90**, 094117 (2014).

[52] D. Y. Song, S. A. Nikishin, M. Holtz, V. Soukhoveev, A. Usikov, and V. Dmitriev, Decay of zone-center phonons in GaN with A_1, E_1, and E_2 symmetries, J. Appl. Phys. **101**, 053535 (2007).

[53] S. Krukowski, A. Witek, J. Adamczyk, J. Jun, M. Bockowski, I. Grzegory, B. Lucznik, G. Nowak, M. Wróblewski, A. Presz, S. Gierlotka, S. Stelmach, B. Palosz, S. Porowski, and P. Zinn, Thermal properties of indium nitride, J. Phys. Chem. Solids **59**, 289 (1998).